Journal of Energy Storage 44 (2021) 103345

Contents lists available at ScienceDirect

Journal of Energy Storage

journal homepage: www.elsevier.com/locate/est

Research Papers

Hierarchical MCo_2O_4@$Ni(OH)_2$ (M = Zn or Mn) core@shell architectures as electrode materials for asymmetric solid-state supercapacitors

Erdenebayar Baasanjav [a], Parthasarathi Bandyopadhyay [a,*], Jung Sang Cho [b,*], Sang Mun Jeong [a,*]

[a] Department of Chemical Engineering, Chungbuk National University, 1 Chungdae-ro, Seowon-Gu, Cheongju, Chungbuk 28644, Republic of Korea
[b] Department of Engineering Chemistry, Chungbuk National University, 1 Chungdae-ro, Seowon-Gu, Cheongju, Chungbuk 28644, Republic of Korea

ARTICLE INFO

Keywords:
Hierarchical
Core@shell
Nitrogen dopped carbon
Solid-state supercapacitor
Energy density

ABSTRACT

In this study, the self-assembled $Ni(OH)_2$-nanosheet-adorned hierarchical MCo_2O_4@$Ni(OH)_2$ (M = Zn or Mn) core@shell heterostructures are prepared by a three-step process, via tuning the core-compositions, as advanced electrodes for supercapacitors (SCs). The tuning of the core composition makes a significant impact on the physicochemical properties, morphology, and electrochemical performance. Among the MCo_2O_4@$Ni(OH)_2$ materials, the nanopine forest-like $ZnCo_2O_4$@$Ni(OH)_2$ optimal architecture exhibits superior supercapacitive performance (areal/specific capacity, 1.34 mA h cm^{-2}/432.6 mA h g^{-1} at 3 mA cm^{-2} current density and a ~90% cycling stability upto 5000 cycles). Meanwhile, 3D porous nitrogen-doped carbon (PNC) with perfect rhombic dodecahedral morphology is used as negative electrode material with high surface area (1600 m^2 g^{-1}), excellent capacity (49.2 mA h g^{-1} at 2 mA cm^{-2}) and rate performance (~55% at 50 mA cm^{-2}). The solid-state asymmetric device comprising $ZnCo_2O_4$@$Ni(OH)_2$ (positive electrode) and hierarchical PNC (negative electrode) affords a high cell capacity of 97.8 mA hg^{-1} at 4 mA cm^{-2}, with 86% cycle stability after 10,000 cycles. Moreover, the device exhibits 78.2 W h kg^{-1} of energy density at a power density of 451 W kg^{-1} and 40.4 W h kg^{-1} of energy density at 4691.0 W kg^{-1} of power density. This study provides insight into electro-active material design and construction of heteronanostructures for high-performance SCs.

1. Introduction

Supercapacitors (SCs) are promising electrochemical energy storage devices that join the gap between traditional capacitors and rechargeable batteries [1,2]. Owing to their low production cost, high charging-discharging efficiency, excellent power density, long cycling lifetime, and environmental benignity, SCs are suitable for a wide range of applications, such as hybrid electrical vehicles, portable electronic materials, and smart electricity grids [3–7]. Current research has concentrated on designing and fabricating advanced SCs that can store a large quantity of energy within a short time. Pseudocapacitive (battery-type) electrode materials are extensively considered as positive electrode materials for SCs. This is because their typical fast redox reactions lead to higher specific capacities and energy densities than those of carbonaceous electrode materials based on the electrochemical double-layer charge-storage reaction mechanism [2,8].

Among the various pseudocapacitive materials, multicomponent transitional metal oxides (TMOs)/hydroxides (TMOHs) are preferentially utilized as electrode material for SCs because of their multiple chemical valence states, structural/morphological flexibility, good electrochemical activity, and low production cost [9–14]. The cobalt-based binary oxides ($MnCo_2O_4$ and $ZnCo_2O_4$) have shown superior electrochemical activity to that of their unitary metal oxide analogues [8,15–17]. However, the voltage window, recharging ability, rate capability, and cycle life of binary TMOs are still mediocre for practical application. Indeed, the foremost challenge of employing binary TMOs as electrode materials for SCs is how to further boost their electrochemical outcome for application in advanced energy-storage devices. An excellent method to resolve these shortfalls is to rationally design and construct multicomponent hybrid complex assemblies using binary TMO-based nanostructures with other pseudocapacitive TMOs/TMOHs on a conductive substrate [8]. Among the different TMOHs, layered nickel hydroxide [$Ni(OH)_2$] is a desirable pseudocapacitive candidate for SCs, owing to its high theoretical capacity, excellent electrochemical

* Corresponding authors.
E-mail addresses: partha012@gmail.com (P. Bandyopadhyay), jscho@chungbuk.ac.kr (J.S. Cho), smjeong@chungbuk.ac.kr (S.M. Jeong).

https://doi.org/10.1016/j.est.2021.103345
Received 11 August 2021; Received in revised form 21 September 2021; Accepted 26 September 2021
Available online 21 October 2021

redox activity, environmental benignity, and availability in different morphologies [17–19]. However, its electrical conductivity, rate performance, and cycling stability are generally unsatisfactory [20–22]. The construction of hierarchical core@shell heterostructures consisting of conductive TMOs as the core (conductive scaffolds/secondary substrate) and $Ni(OH)_2$ as the shell layer is a unique approach to overcome the limitations of individual materials and fully utilize their advantages. Hybrid hierarchical heterostructures prepared from binary TMOs and $Ni(OH)_2$ have already been reported. Zhao et al. created $MnCo_2O_4$@$Ni(OH)_2$ nanoflowers as a positive electrode material for SCs. The electrode demonstrated a specific capacitance (C_{SP}) of 2154 F g^{-1} at 5 A g^{-1} and a rate performance of 32.6% at 20 A g^{-1} [8]. Liu et al. synthesized $MnCo_{2}O_{4.5}$@$Ni(OH)_2$, a flower-like electrode that exhibited a C_{SP} value of 2544.44 F g^{-1} at 3 A g^{-1} and 82.8% rate performance up to 20 A g^{-1}, with 87.7% cyclic stability after 5000 cycles [17]. Wu et al. synthesized a hierarchical CoO@$Ni(OH)_2$ nanostructure electrode that exhibited a C_{SP} of 1418.2 F g^{-1} at 1 A g^{-1} and a rate capability of 65% at 10 A g^{-1}, with a cycle stability of 93.7% after 5000 consecutive cycles [19]. Li et al. developed $CoMoO_4$@$Ni(OH)_2$ material onto Ni-modified surfaces and channels of a well-ordered macroporous silicon electrode plate for SCs [20]. The electrode showed a C_{SP} value of 1812.42 F g^{-1} at 2 mA cm^{-2} and a rate performance of 45.9% at 32 mA cm^{-2}, with a lifespan of 87.42% after 5000 cycles. Zhu et al. synthesized carbon cloth-supported $CuCo_2O_4$@$Ni(OH)_2$ hybrid material as a positive electrode for SCs, which delivered a C_{SP} of 2160 F g^{-1} at 1 A g^{-1}, 82.7% capacitance retention up to 20 A g^{-1}, and 92% cyclic stability up to 5000 cycles [18]. However, the above TMO@$Ni(OH)_2$ core@shell materials cannot fulfill the requirements for superior energy storage devices. To date, the maintenance of ultra-high specific capacity and excellent rate capability and cycle life of TMO@$Ni(OH)_2$ heterostructures remains a crucial challenge. The hetero-growth of mixed TMO- and TMOH-based core@shell structures is challenging to control because of their apparent structural diversity, which results in improper morphology and structure and poor electrochemical properties. More importantly, the above-mentioned literature survey clearly illustrates that although the shell was based on $Ni(OH)_2$ in each core@shell material, the synthetic method of the $Ni(OH)_2$ shell preparation was different in each case. Therefore, the assimilation of $Ni(OH)_2$ shell onto different TMO core materials with different structural features, for SC application through a similar synthetic protocol, is highly desirable.

With these facts in mind, in this study, we rationally designed and successfully fabricated hierarchical MCo_2O_4@$Ni(OH)_2$ (M = Zn or Mn) core@shell architectures on Ni-foam (NF) by varying the composition of core materials (MCo_2O_4) via similar experimental condition. The primary objectives and merits of the present study are as follows: (i) The assembly of a core@shell structure consisting of different core compositions and a fixed shell is valuable in realizing the required electrochemical storage performance based on structural and morphological features. The hierarchical conductive MCo_2O_4 (M = Zn or Mn) nanowire arrays (NWs) grown directly on conductive NF act as the backbone and "electronic superhighway medium" for charge transport and storage, overcoming the low conductivity of the shell [19]. In this context, the selection of a suitable bimetallic oxide core can enable to boost the electrochemical performance. (ii) The thickness of the shell material strongly influences the supercapacitive performance of the core@shell [23]. Therefore, the thickness of the $Ni(OH)_2$ nanosheets was tuned by changing the hydrothermal shell growth reaction times to obtain optimum shell thickness. (iii) The hierarchical core@shell materials are grown directly onto the 3D NF, which enhances the electrical conductivity and also helps to reduce the ion-diffusion path length at the electrode/electrolyte interface.

Among the prepared MCo_2O_4@$Ni(OH)_2$ materials, $ZnCo_2O_4$@$Ni(OH)_2$ exhibited the finest morphology, highest specific surface area (SA), and superior electrochemical performance. Thus, the $ZnCo_2O_4$@$Ni(OH)_2$ NW array as positive electrode was then used to assemble an asymmetric SC (ASC) device, in which KOH/PVA and the 3D ZIF-8-derived porous nitrogen-based carbon (PNC) served as the gel-electrolyte and negative electrode material, respectively. The asymmetric solid-state device exhibited an outstanding combination of energy and power densities together with a long cycle life.

2. Experimental section

2.1. Synthesis of M-Co-oxide nanowire arrays (MCo_2O_4 NWs; M = Zn or Mn)

The NFs were cleaned thoroughly according to our reported literature [3,5]. The MCo_2O_4 NWs on the NF substrate were grown by an easy hydrothermal reaction method followed by calcination. In brief, an aqueous precursor solution of $Co(NO_3)_2{\cdot}6H_2O$ (0.291 g), $Zn(NO_3)_2{\cdot}6H_2O$ (0.149 g), urea (0.180 g), and ammonium fluoride (0.037 g) was gently stirred for 15 min to dissolve all the precursor materials. The resultant solution was poured into a Teflon-lined steel autoclave containing a cleaned NF piece. After sealing the autoclave properly, the hydrothermal reaction was carried out at 120 °C for 6 h. Subsequently, the autoclave temperature was allowed to decrease naturally to room temperature (25–30 °C), and the resulting Zn-Co hydroxide precursor NW arrays (Zn-Co LDH NWs)-coated NF was picked out, cleaned, and subsequently dried for 24 h at 60 °C. After calcination at 350 °C for 2 h, the precursor NWs were transformed into $ZnCo_2O_4$ NWs. The $MnCo_2O_4$ NWs were also fabricated by a similar method, replacing the Zn salt with the Mn salt. The average deposited masses of $ZnCo_2O_4$ and $MnCo_2O_4$ NWs onto the NF were measured to be 2.2 and 1.4 mg cm^{-2}, respectively.

2.2. Synthesis of hierarchical MCo_2O_4@$Ni(OH)_2$ (M = Zn or Mn) core@shell nanohybrid arrays

The $Ni(OH)_2$ nanosheets were grown onto to the $ZnCo_2O_4$ core material using different hydrothermal reaction time (0.5, 1, and 2 h) for shell synthesis to obtain an optimal shell thickness. In a typical optimized synthesis procedure of $ZnCo_2O_4$@$Ni(OH)_2$, a measured amount of $NiCl_2{\cdot}6H_2O$ and urea was added to distilled water and then stirred for 15 min to make a uniform solution. Then, the mixed solution was transferred into a Teflon-lined autoclave and a piece of $ZnCo_2O_4$ NW array (M = Zn or Mn)-coated NF was dipped into the solution. The autoclave was properly sealed and kept at 100 °C for 1 h. After cooling the autoclave, the resultant NF supported $ZnCo_2O_4$@$Ni(OH)_2$ sample was cleaned and maintained in an oven at 65 °C for 24 h. For comparison, the $MnCo_2O_4$@$Ni(OH)_2$ sample was also synthesized using a similar method as mentioned above. The mass loadings of $ZnCo_2O_4$@$Ni(OH)_2$ and $MnCo_2O_4$@$Ni(OH)_2$ nanoarrays were found to be 3.1 and 2.3 mg/cm^2, respectively.

2.3. Synthesis of ZIF-derived porous nitrogen-doped carbon (PNC)

The 3D ZIF-8-derived porous nitrogen-based carbon was synthesized and used as a negative electrode. First, $Zn(CH_3COO)_2{\bullet}2H_2O$ (4 mmol) and 2-methylimidazole (24.0 mmol) were separately dissolved by magnetic stirring in 35 mL and 15 mL methanol, respectively. Both solutions were separately kept on a ice-cold water chamber for 1 h. Next, the imidazole solution was added dropwise to the uniform solution of zinc acetate and then stirred at 25 °C for 10 min. Subsequently, the mixed solution was aged for 24 h at 25 °C. The as-obtained white ZIF-8 precipitate was then suspended in absolute ethanol, collected by centrifugation, and finally freeze-dried for 2 d The PNC material was obtained as a black powder by annealing the ZIF-8 particles for 3 h at 800 °C under nitrogen atmosphere.

2.4. Material characterizations

The crystallinity of the manufactured samples was determined by X-

ray diffraction (XRD; D8 Discover with GADDS, Bruker AXS) with Cu Kα radiation (wavelength: 0.54 Å). The chemical compositions and valence states of the synthesized materials were analyzed by XPS (PHI Quantera-II, Ulvac-PHI). The surface morphological characteristics, structures, and compositions were analyzed using a field emission scanning electron microscopy (FESEM) analysis (Carl Zeiss, LEO-1530). To further scrutinize the morphology of the electro-active material, transmission electron microscopy (TEM) analysis (low and high magnification), selected area electron diffraction (SAED), and energy-dispersive X-ray (EDX) spectroscopy mapping were carried out using a JEM-2100F (UHR, JEOL). To determine the surface properties (SA and porosity), nitrogen (N_2)-sorption isotherms were collected on a Micromeritics (ASAP 2420) gas sorption analyzer at 77 K.

2.5. Electrochemical characterizations

Electrochemical analyses of all the electro-active materials (working electrode) were performed using an electrochemical workstation (AUT88370, PGSTAT302N, Netherlands) in a three-electrode assembly. The Pt sheet and Ag/AgCl (KCl saturated) served as the counter (auxiliary) and reference electrodes, respectively, in a 2 M aqueous KOH solution. The NF-supported as-synthesized samples were directly used as the binder-free working electrode (area = 1 cm × 1 cm). The negative electrode (PNC) was made via a typical slurry-based method using a NF substrate, as reported in the literature [4]. EIS was performed over a frequency range of 10^5–10^{-2} Hz at open circuit potential. An ASC device was constructed utilizing $ZnCo_2O_4$@$Ni(OH)_2$ nanohybrid positive and PNC negative electrodes and KOH/PVA as the solid electrolyte. Notably, the weight ratio between the negative and positive electrode materials in the device was determined to be ~4.0, based on the typical three-electrode performance of each electrode. Total electroactive material mass of the two electrodes (negative and positive electrodes) for the device fabrication was 8 mg.

The gel electrolyte (KOH/poly(vinyl alcohol) (PVA)) was prepared as follows: 3 g of PVA powder and 1.5 g of KOH were dissolved in distilled water (30 mL). Then, the whole solution mixture was continuously stirred for 1 h at 90 °C. Next, the $ZnCo_2O_4$@$Ni(OH)_2$, PNC electrodes and Whatman 42 filter paper (separator) were soaked in KOH/PVA gel electrolyte for ~ 20 mint. Then, both the electrodes were assembled along with the separator and allowed to solidify under ambient temperature for ~ 24 h. The as-fabricated ASC device was placed properly into a split test cell for electrochemical study. The specific capacity (S_C) and areal capacity (S_A) were calculated using the following formulas [5,12]:

$$S_C = \frac{2I\int Vdt}{mV} \quad (1)$$

$$S_A = \frac{2I\int Vdt}{AV} \quad (2)$$

where I is the current applied, m is the mass loading, A is the area with deposited mass (1 cm × 1 cm), and V is the potential range; $\int Vdt$ is integral area under the discharge plot. Moreover, since the ASC device is a typical two-electrode assembly, m represents the overall masses of the active materials of the negative and positive electrodes.

The energy density (E_D) and power density (P_D) of the device were evaluated by the following equations:

$$E_D = \frac{I\int Vdt}{m \times 3.6} \quad (3)$$

$$P_D = \frac{E \times 3600}{t} \quad (4)$$

where the time of discharge is denoted as 't'.

3. Results and discussion

The synthesis route for the fabrication of the core@shell material is schematically shown in Fig. 1. The 3D hierarchical NW arrays of the M-Co layered double hydroxide (M-Co LDH; M = Zn or Mn) precursors were grown onto the NF using a hydrothermal reaction in the presence of the metal precursor salt, urea, and ammonium fluoride. Next, the M-Co LDH NW arrays were annealed at 350 °C via a complex air oxidation procedure to construct the MCo_2O_4 NWs-coated NF. The as-obtained rough MCo_2O_4 NWs were then used as the skeleton support to grow ultra-thin $Ni(OH)_2$ nanosheets during another hydrothermal reaction, driven by surface-energy reduction, to form MCo_2O_4@$Ni(OH)_2$ nanohybrids.

The architectures and surface morphologies of the NF-supported MCo_2O_4 NWs and MCo_2O_4@$Ni(OH)_2$ nanohybrids were investigated by field emission scanning electron microscopy (FESEM) analysis. Fig. 2a, d show the FESEM images of $ZnCo_2O_4$ and $MnCo_2O_4$, respectively. The entire NF surface is fully coated by the MCo_2O_4 NWs after hydrothermal reaction and successive calcination. The FESEM images reveal that the MCo_2O_4 NWs are highly aligned on the substrate, providing an ideal platform for the formation of $Ni(OH)_2$ sheets. The oxide NWs show porous architecture, attributed to the elimination of H_2O and CO_2 during calcination. High- and low-magnification FESEM imagery of the $ZnCo_2O_4$@$Ni(OH)_2$ nanohybrid arrays are shown in Fig. 2b and c, respectively, which reveal that the diameters of the $ZnCo_2O_4$@$Ni(OH)_2$ heterostructures increase and the surfaces of the nanohybrids become wrinkled after assimilation of the $Ni(OH)_2$ sheets onto the oxide NW arrays. In addition, the $ZnCo_2O_4$ NWs retain their inherent structural features after being orderly and uniformly decorated by the $Ni(OH)_2$ sheets in the final core@shell structures. Notably, no Ni$(OH)_2$ nanosheets are observed between the NWs, and the interconnected ultra-thin $Ni(OH)_2$ nanosheets uniformly cover the outer surface of the $ZnCo_2O_4$ NWs in a twisting and crumpling manner. This produce a unique 3D hierarchical highly porous core@shell architecture. The distances between the adjacent interconnected nanosheets generate voids, resulting in an interconnected architecture that is ideal for fast electron transportation and ion diffusion [2,12]. Such a distinctive hierarchical architecture with open and free interspaces between the nanosheets enhances the area of contact between the electrolyte and electrode material and enables easy access of the electrolytes to the core materials. Furthermore, the combination of a $Ni(OH)_2$ shell layer onto the 3D hierarchical $ZnCo_2O_4$ NW protects the core material during long-run charging-discharging cycles [19]. In contrast, in $MnCo_2O_4$@$Ni(OH)_2$, the neighboring $Ni(OH)_2$ sheets are in contact with each other, owing to the limited space between them. The thick/dense $Ni(OH)_2$ nanosheet layer on the surfaces of the $MnCo_2O_4$ NWs can entirely mask the core material (Fig. 2e, f). Furthermore, $Ni(OH)_2$ sheets were deposited within the gaps of the $MnCo_2O_4$ NWs, resulting in the agglomerated morphology of the $MnCo_2O_4$@$Ni(OH)_2$ nanohybrid.

All the materials presented three strong XRD peaks at 44.68, 52.09, and 76.61°, ascribed to the typical XRD peaks of the NF (Fig. 3) [3]. The XRD peaks of the as-prepared $ZnCo_2O_4$ NWs are well-identified with JCPDS card 00–001–1149 of cubic $ZnCo_2O_4$ (Fig. 3a). The XRD patterns of the as-fabricated $MnCo_2O_4$ NWs (Fig. 3b) are similar to those of the planes of cubic $MnCo_2O_4$, as reported in JCPDS card 00–001–1130. The characteristic XRD pattern of $Ni(OH)_2$, as reported in JCPDS card 00–003–0177, shows the most prominent peaks at 19.58°, assigned to the (001) plane. Other peaks at 33.40° and 38.78°, corresponding to the (100) and (101) planes, respectively, are also observed. These major Ni$(OH)_2$ and $ZnCo_2O_4$ diffraction peaks are noticed in the XRD patterns of $ZnCo_2O_4$@$Ni(OH)_2$ (Fig. 3a). Similarly, the diffraction pattern of $MnCo_2O_4$@$Ni(OH)_2$ shows the presence of $Ni(OH)_2$ and $MnCo_2O_4$ (Fig. 3b). The peak positions related to the $Ni(OH)_2$ present in the core@shell material are broad, owing to the very small crystalline sizes of $Ni(OH)_2$ [24]. In comparison to the XRD diffraction peaks of $ZnCo_2O_4$@$Ni(OH)_2$, the peaks of $MnCo_2O_4$ are less prominent in the

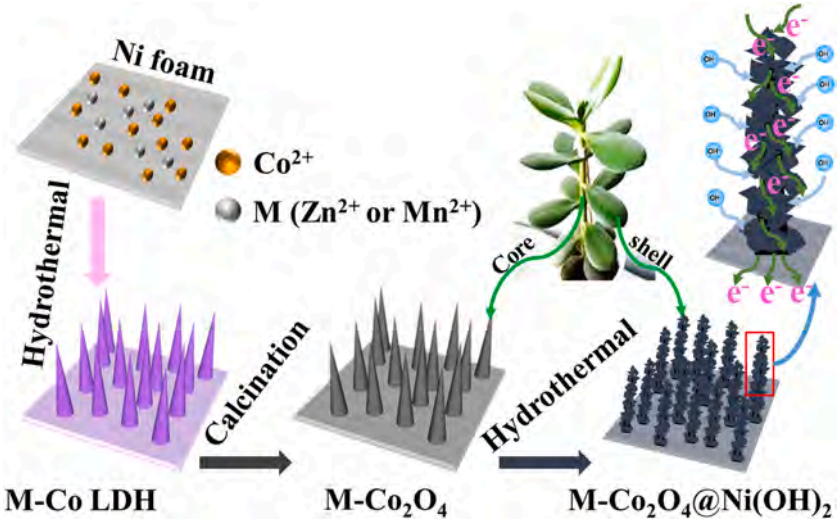

Fig. 1. Schematic illustration of the synthesis of hierarchical MCo_2O_4@$Ni(OH)_2$ (M = Zn or Mn) core@shell nanostructures.

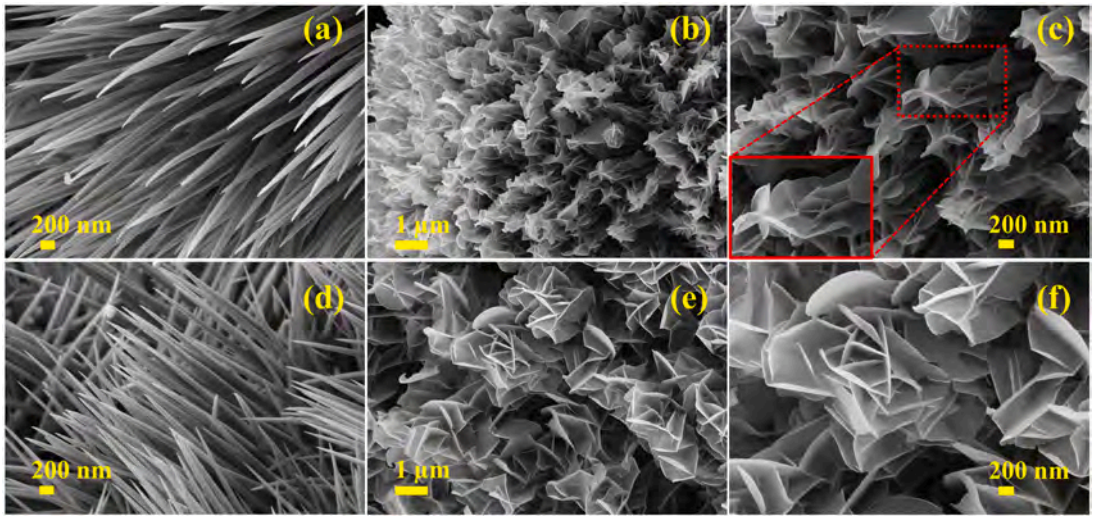

Fig. 2. FESEM images of the (a) $ZnCo_2O_4$ nanowire arrays, (b, c) $ZnCo_2O_4$@$Ni(OH)_2$ nanohybrid, (d) $MnCo_2O_4$ nanowire arrays, and (e, f) $MnCo_2O_4$@$Ni(OH)_2$ nanohybrid.

$MnCo_2O_4$@$Ni(OH)_2$ XRD pattern. In this case, the excess growth of the $Ni(OH)_2$ shell overshadow the $MnCo_2O_4$ peaks, corroborating the FESEM image. Peak shifting of the MCo_2O_4 and $Ni(OH)_2$ materials is observed in our as-synthesized core@shell materials, as compared to their corresponding JCPDS patterns. XRD peak position shifting is generally found in multicomponent hybrid materials, and slightly shifted peak positions of $Ni(OH)_2$ over their related JCPDS patterns have been previously reported [17,24–26].

Because the SA, pore-diameter, and pore size distribution are important factors for electro-active nanostructured materials, Brunauer–Emmett–Teller (BET) nitrogen adsorption–desorption analyses were performed to evaluate these properties. The N_2 adsorption and desorption isotherms of all the samples were plotted and are shown in Fig. 3c and S1a. A characteristic IV-type isotherm with a distinct hysteresis loop is observed for all samples within the relative pressure ranging from 0.45 to 1.0 P/P_0, indicating their mesoporous character [22]. The BET specific SA values of $ZnCo_2O_4$, $ZnCo_2O_4$@$Ni(OH)_2$, $MnCo_2O_4$, and $MnCo_2O_4$@$Ni(OH)_2$ are determined as 62.0, 91.0, 60.7, and 70 $m^2\ g^{-1}$, respectively. An increment in the specific SA of the core@shell material is attributed to the presence of interconnected $Ni(OH)_2$ nanosheets on the core surface [2]. The high BET specific SA is advantageous for delivering more electro-active area for redox reaction. The pore-size distribution analyses of all the samples were performed using the Barrett-Joyner-Halenda (BJH) method, and the corresponding distribution analysis outcomes are displayed in Fig. 3d and S1b. These data show that the average pore size distributions for $ZnCo_2O_4$, $ZnCo_2O_4$@$Ni(OH)_2$, $MnCo_2O_4$, and $MnCo_2O_4$@$Ni(OH)_2$ are mainly centered at 3.87, 3.66, 3.92, and 3.95 nm, respectively, indicating the excellent mesoporosity of all these materials. The total pore volumes of $ZnCo_2O_4$, $ZnCo_2O_4$@$Ni(OH)_2$, $MnCo_2O_4$, and $MnCo_2O_4$@$Ni(OH)_2$ are determined as 0.14, 0.38, 0.13, and 0.20 $cm^3\ g^{-1}$, respectively. Specifically, $ZnCo_2O_4$@$Ni(OH)_2$ possesses the higher SA than the reported analogous core@shell material [2,17,19,20]. The high SA and pore volume expose more of the electro-active site for mass transport and redox reaction, thereby improving the charge-storage capacity of $ZnCo_2O_4$@$Ni(OH)_2$.

The detailed morphology of the $ZnCo_2O_4$ and $ZnCo_2O_4$@$Ni(OH)_2$ structures were further studied by transmission electron microscopy (TEM). The TEM image of a single $ZnCo_2O_4$ NW exhibits the porosity ascribed to the annealing of its mother element Zn-Co LDH (Fig. 4a). Notably, the TEM image (Fig. 4b) of $ZnCo_2O_4$@$Ni(OH)_2$ shows that the ultra-thin $Ni(OH)_2$ sheets are anchored onto the $ZnCo_2O_4$-embedded NF,

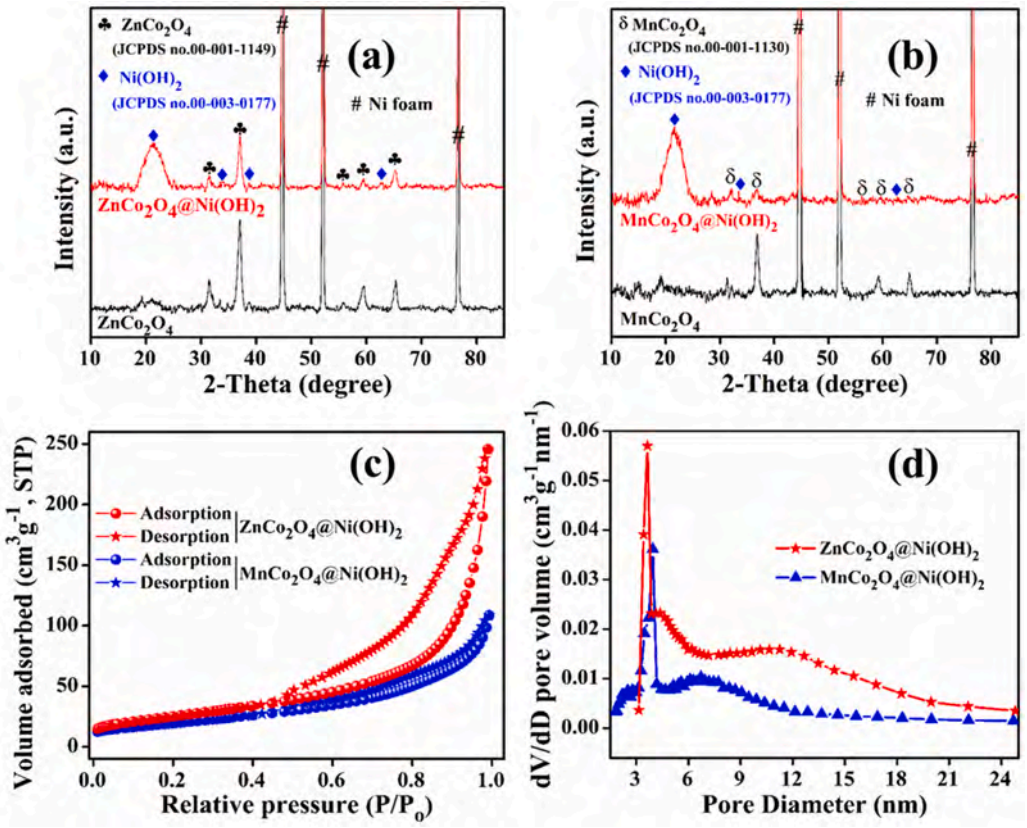

Fig. 3. (a) XRD patterns of (a) $ZnCo_2O_4$ and $ZnCo_2O_4$@$Ni(OH)_2$ and (b) $MnCo_2O_4$ and $MnCo_2O_4$@$Ni(OH)_2$. Plots of (c) N_2 sorption isotherms and (d) pore size distributions (BJH plots) of $ZnCo_2O_4$@$Ni(OH)_2$ and $MnCo_2O_4$@$Ni(OH)_2$.

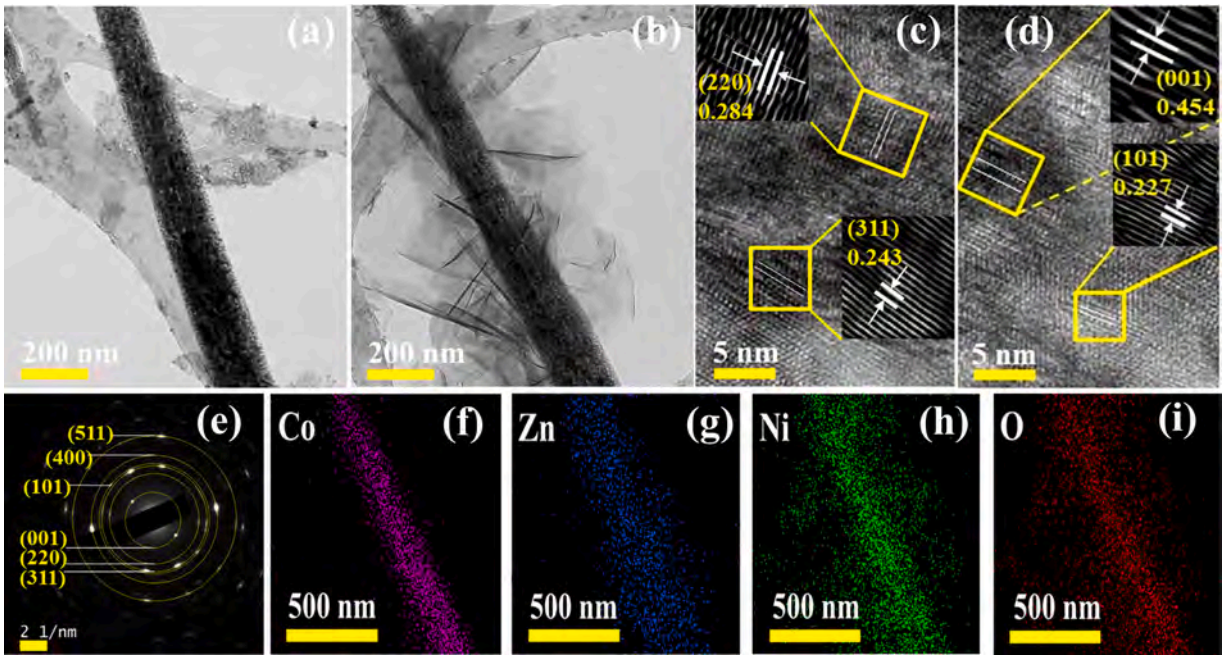

Fig. 4. (a) TEM image of $ZnCo_2O_4$ nanowire. (b) TEM images of the $ZnCo_2O_4$@$Ni(OH)_2$ nanohybrid. (c) HRTEM images of the $ZnCo_2O_4$ core area. (d) HRTEM image of the $Ni(OH)_2$ shell area. (e) SAED pattern of the $ZnCo_2O_4$@$Ni(OH)_2$ nanohybrid. EDX color mapping for (f) Co, (g) Zn, (h) Ni, and (i) O.

forming a unique core@shell architecture. The porous $Ni(OH)_2$ nanosheets with a average thickness of ~ 200 nm are uniformly grown over the $ZnCo_2O_4$ NW. This architecture reinforces $Ni(OH)_2$ nanosheet surfaces, providing more electro-active sites for electrochemical reaction. The fabrication of such unique $ZnCo_2O_4$@$Ni(OH)_2$ nanohybrid improves the conductivity and electron transport, thus boosting the rate performance and cyclic stability. The $ZnCo_2O_4$@$Ni(OH)_2$ shows fringe spacings of ~0.243 and 0.284 nm assigned to the (311) and (220) planes of

$ZnCo_2O_4$, respectively, (Fig. 4c). The lattice spacings of ~0.454 and 0.227 nm are ascribed to the (001) and (101) crystal planes of $Ni(OH)_2$, respectively, (Fig. 4d). The SAED pattern of the core@shell material reveals bright spots and a typical ring pattern, demonstrating its crystalline character, and the diffraction rings are ascribed to the (311), (220), and (511) planes of $ZnCo_2O_4$ and (001) and (101) planes of $Ni(OH)_2$, as shown in Fig. 4e. Furthermore, EDX elemental mapping (Fig. 4f-i) confirms that the elements Zn and Co are concentrated in the core region, whereas O and Ni are dispersed in the whole area, thereby indicating $ZnCo_2O_4$@$Ni(OH)_2$ core@shell heterostructure formation.

X-ray photoelectron spectroscopy (XPS) was performed to attain further insight into the elemental oxidation states and compositions of $ZnCo_2O_4$@$Ni(OH)_2$ and $MnCo_2O_4$@$Ni(OH)_2$ materials. The survey spectra (Figs. S2a, b) of $ZnCo_2O_4$@$Ni(OH)_2$ and $MnCo_2O_4$@$Ni(OH)_2$ show the presence of the elements Co, Zn, Ni, and O and Co, Mn, Ni, and O, respectively. The Co 2p XPS spectrum (Fig. 5a) of $ZnCo_2O_4$@$Ni(OH)_2$ exhibits two prominent peaks at ~795.3 and 780.0 eV, corresponding to the Co $2p_{1/2}$ and Co $2p_{3/2}$, respectively, and two shake-up satellite peaks (identified as Sat.) [17,19,27,28]. Similarly, the deconvoluted Co 2p spectrum of $MnCo_2O_4$@$Ni(OH)_2$ displays two peaks at binding energy of 796.3 (Co $2p_{1/2}$) and 780.6 (Co $2p_{3/2}$) eV, and two shake-up satellite peaks. Therefore, the Co 2p XPS spectra analyses confirm the presence of Co^{2+} and Co^{3+} states in $ZnCo_2O_4$@$Ni(OH)_2$ and $MnCo_2O_4$@$Ni(OH)_2$ materials. The XPS Zn 2p spectrum of $ZnCo_2O_4$@$Ni(OH)_2$ can be divided into two prominent peaks assigned to the Zn $2p_{3/2}$ (1022.6 eV) and Zn $2p_{1/2}$ (1045.7 eV) states, as shown in Fig. 5b [12]. It can be observed from the Fig. 5c that the Mn 2p spectrum is split into two peaks which are identified as Mn $2p_{1/2}$ and Mn $2p_{3/2}$ levels. The XPS Mn 2p spectrum pattern is nicely corelated with reported literature [29–32].The broad Mn $2p_{3/2}$ peak pattern suggests the probable charging effects and multiplet splitting have resulted in the line broadening [33]. The Ni 2p deconvoluted spectra of $ZnCo_2O_4$@$Ni(OH)_2$ and $MnCo_2O_4$@$Ni(OH)_2$ display two peaks at binding energies of ~855.6 and 873.5 eV, assigned to the Ni $2p_{3/2}$ and Ni $2p_{1/2}$ states (Fig. 5d), respectively [3,5]. Another two peaks at 861.7 and 879.5 eV are assigned as the shake-up satellite peaks of the Ni^{2+} ion. Fig. 5e show the deconvoluted O1s spectra of $ZnCo_2O_4$@$Ni(OH)_2$ and $MnCo_2O_4$@$Ni(OH)_2$, respectively, where the two peaks at ~530.4 and 532.6 eV are attributed to the O^{2-} ion in metal oxide phase and hydroxyl group, respectively, [17,19,31,34].

The electrochemical performances of all the binder-free NF-supported samples were investigated in a three-electrode measuring assembly using a 2 M aqueous KOH solution. The $ZnCo_2O_4$ NWs were used as a perfect scaffold to fabricate the complex core@shell architecture of $ZnCo_2O_4$@$Ni(OH)_2$. To obtain an optimal $Ni(OH)_2$ shell thickness on the $ZnCo_2O_4$ core, the shell was synthesized with varying hydrothermal reaction times (0.5, 1, and 2 h). Then, the tuning effect of the shell-formation reaction time on the electrochemical performance of the core@shell material was monitored by cyclic voltammetry (CV) and galvanostatic charge-discharge (GCD) analyses (Fig. S3). Accordingly, the electrochemical performances of these samples were co-related with their FESEM images to understand the role of shell thickness in manipulating the supercapacitive performance. Comparison of the electrochemical performances clearly indicates that a 0.5 h shell growth reaction time is insufficient to develop a uniform $Ni(OH)_2$ shell layer onto the $ZnCo_2O_4$ NW arrays (Figs. S4a-c). Accordingly, the core@shell material formed for the 0.5 h of shell-formation reaction time shows minimum capacity. A reaction time of 1 h is deemed optimal for the development of uniform $Ni(OH)_2$ shell layer over the core material. The well-covered $Ni(OH)_2$ shell layer allows easy infiltration of the electrolyte ions in the $ZnCo_2O_4$ NW arrays to deliver the maximum electrochemical outcome of the core@shell heterostructure (Fig. 2b-c). However, with the further increase in the hydrothermal reaction time to 2 h, the afforded $ZnCo_2O_4$@$Ni(OH)_2$ exhibits decreased supercapacitive performance due to the increase in shell thickness (Figs. S4d-f). As the Ni $(OH)_2$ shell thickness/density increases with increasing reaction time, the contribution of the core material to the overall capacity decreases. This is attributed to the higher shell thickness, which inhibits the uniform access of the electrolyte to the $ZnCo_2O_4$ NW arrays and decreases the overall electrochemical outcome of the $ZnCo_2O_4$@$Ni(OH)_2$ material. Hence, a hydrothermal reaction time of 1 h was selected as the optimum

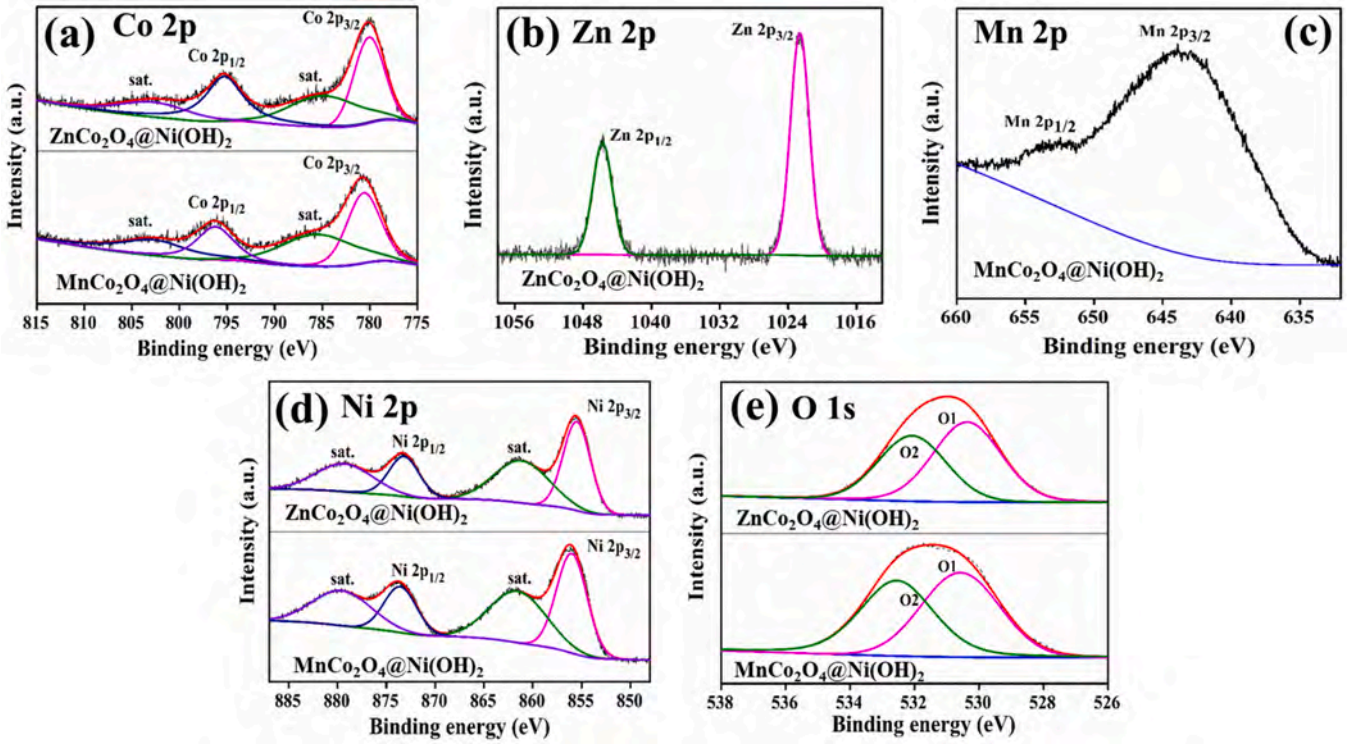

Fig. 5. XPS analyses: (a) Co 2p spectra for $ZnCo_2O_4$@$Ni(OH)_2$ and $MnCo_2O_4$@$Ni(OH)_2$, (b) Zn 2p spectrum of $ZnCo_2O_4$@$Ni(OH)_2$, (c) Mn 2p spectrum of $MnCo_2O_4$@$Ni(OH)_2$, (d) Ni 2p spectra of $ZnCo_2O_4$@$Ni(OH)_2$ and $MnCo_2O_4$@$Ni(OH)_2$, and (e) O 1 s spectra of $ZnCo_2O_4$@$Ni(OH)_2$ and $MnCo_2O_4$@$Ni(OH)_2$.

time to obtain perfect growth of the $Ni(OH)_2$ shell layer onto the $ZnCo_2O_4$ core, and $MnCo_2O_4$@$Ni(OH)_2$ was fabricated by following a similar synthesis protocol for comparison.

The CV plots of $ZnCo_2O_4$@$Ni(OH)_2$, $MnCo_2O_4$@$Ni(OH)_2$, $ZnCo_2O_4$, and $MnCo_2O_4$ at 10 mV s^{-1}, across a potential range of 0.2–0.75 V were next investigated and compared (Fig. 6a). In each cathodic and anodic scan, all the electrode samples show distinct redox peaks, revealing their battery-type character and that the capacity is mainly governed by a redox mechanism [8,19]. The oxidation/reduction peaks located at ~0.48/0.13, 0.43/0.15, 0.34/0.18, and 0.31/0.21 V (vs Ag/AgCl), observed at a scanning rate of 10 mV s^{-1}, are assigned to the electrochemical Faradaic reactions of the $ZnCo_2O_4$@$Ni(OH)_2$, $MnCo_2O_4$@$Ni(OH)_2$, $ZnCo_2O_4$, and $MnCo_2O_4$ electrodes, respectively. The representative oxidation/reduction peaks of $ZnCo_2O_4$ and $MnCo_2O_4$ are primarily ascribed to the reversible electron transfer processes between the different valance states of the Co ion (Co^{2+}/Co^{3+}). However, for the core@shell material, the analogous oxidation and reduction peaks are due to the Faraday reversible redox reactions of Co^{2+}/Co^{3+} (core material) and Ni^{2+}/Ni^{3+} (shell material) in the presence of aqueous KOH solution [2]. As a result, compared to the $ZnCo_2O_4$ and $MnCo_2O_4$, the assimilation of the $Ni(OH)_2$ shell onto the MCo_2O_4 NWs results in a higher current density and larger integrated CV curve area. Fig. 6b shows the CV outputs of $ZnCo_2O_4$@$Ni(OH)_2$ at separate sweep rates (5–50 mV s^{-1}) within a fixed potential width range of −0.2 to 0.75 V. The typical reduction/oxidation peaks slightly shifted toward more negative and positive potential directions, respectively, upon raising the scan rate, which is attributed to the active material polarization [22,35]. This also shows that the electro-active material exhibits a quick oxidation–reduction reaction at the electrode/electrolyte junction with the increase in current density. Moreover, the absence of any significant variations in the shapes of the CV curves suggests a superb rate performance and good reversible redox reaction of $ZnCo_2O_4$@$Ni(OH)_2$ electrode [12]. Compared to the other samples, $ZnCo_2O_4$@$Ni(OH)_2$ contributes to a larger integrated area under the current vs potential curve, indicating its superior specific/areal capacity. The excellent synergetic interaction between the 1D $ZnCo_2O_4$ NWs and optimized ultra-thin 2D $Ni(OH)_2$ shell results in better electronic conductivity and electrochemical outputs. Furthermore, $ZnCo_2O_4$@$Ni(OH)_2$ exhibits the highest effective SA with a smaller pore size, thereby providing a more electrochemically active SA for facile electron and ion transport at the electrolyte/electrode junction. More importantly, the presence of Zn element improves the electrical conductivity, mechanical flexibility, and chemical stability of the bimetallic oxide, thereby providing good mechanical support and electron transport channels to enhance the electrochemical storage capability of the $ZnCo_2O_4$@$Ni(OH)_2$ heterostructures [36].

Fig. S5 illustrates that the plots of the peak current density (I_p; anodic/cathodic) values versus square root of the scan rates ($\nu^{1/2}$) at different scan rates for the $ZnCo_2O_4$@$Ni(OH)_2$ and $MnCo_2O_4$@$Ni(OH)_2$ electrodes. These plots show a linear relationship between I_p and $\nu^{1/2}$ and properly match with the typical power-law relationship ($I_p = a\nu^b$, where $b = 0.5$), suggesting a fully diffusion-controlled Faradaic reaction process for both the electrodes [37–40].

GCD measurements of all the samples at different current densities (3–50 mA cm^{-2}), over the fixed potential window range of 0–0.45 V, were performed to compare their electrical charge-storage performances. The typical GCD plots of the $ZnCo_2O_4$@$Ni(OH)_2$ core@shell material and other electrode materials are shown in Figs. 6c and S6, respectively. A consistent but divergent potential plateau area can be observed during the charging and discharging processes of all these samples, confirming their battery-type character, thereby corroborating with the CV results [41]. Furthermore, all the studied electrode materials display approximately symmetrical GCD curves at varied current densities, indicating the excellent reversibility of the Faraday reaction process and good capacitive characteristics [11]. The discharge time for the four electrodes follow the order: $MnCo_2O_4$ < $ZnCo_2O_4$ < $MnCo_2O_4$@$Ni(OH)_2$ < $ZnCo_2O_4$@$Ni(OH)_2$. To verify the superiority of the $ZnCo_2O_4$@$Ni(OH)_2$ sample over the $MnCo_2O_4$@$Ni(OH)_2$, $ZnCo_2O_4$, and $MnCo_2O_4$ samples, we determined the specific and areal capacities from the discharge part of the GCD plot. The areal/specific capacity values of all these samples at various areal current densities are depicted in Fig. 6d. The higher capacity value of the core@shell materials are ascribed to the increased electrochemical active SA and additional capacity supplied by $Ni(OH)_2$. The synergetic effect within the heteronanostructure enhanced the charge-transfer process, thus improving the energy storage efficacy of the electro-active material [18]. Notably, the areal and specific capacity values of the $ZnCo_2O_4$@$Ni(OH)_2$ electrode are much higher than the other electrodes at different current densities.

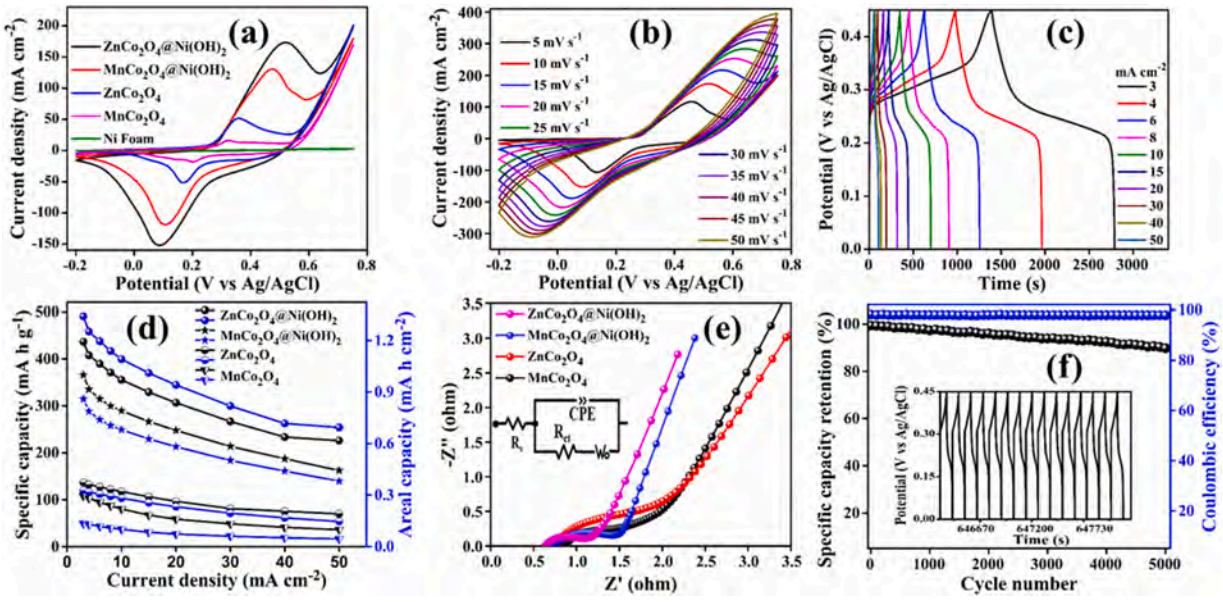

Fig. 6. (a) CV curves of $ZnCo_2O_4$, $MnCo_2O_4$, $MnCo_2O_4$@$Ni(OH)_2$, and $ZnCo_2O_4$@$Ni(OH)_2$ at 10 mV s^{-1}. (b) CV curves of the $ZnCo_2O_4$@$Ni(OH)_2$ electrode at different scan rates. (c) Galvanostatic charge-discharge (GCD) plots of the $ZnCo_2O_4$@$Ni(OH)_2$ electrode at different current densities. (d) Plot of specific/areal capacity vs current density for all the electrodes. (e) EIS Nyquist plots for all the electrodes at open circuit voltage (inset: equivalent circuit used to fit the data). (f) Cyclic performance and Coulombic efficiency of $ZnCo_2O_4$@$Ni(OH)_2$ at a current of 40 mA cm^{-2} (inset: final 15 GCD cycles).

The $ZnCo_2O_4$@$Ni(OH)_2$ core@shell electrode shows superior areal capacity values as high as ~1.34, 1.25, 1.20, 1.14, 1.09, 1.01, 0.94, 0.82, 0.72, and 0.69 mA h cm^{-2} under current densities of 3, 4, 6, 8, 10, 15, 20, 30, 40, and 50 mA cm^{-2}, respectively. The corresponding specific capacity values of this sample are ~ 432.6, 404.0, 386.0, 367.5, 352.0, 326.2, 303.8, 264.3, 231.3, and 224.0 mA h g^{-1}. All these electrodes show a decreasing trend in the capacity values with increasing areal current densities, owing to their internal resistances. Moreover, at higher current, the outer surface pores are mainly utilized, while most of the deeper electro-active pores are inaccessible during fast electrochemical reaction [22]. The capacity retention values of $ZnCo_2O_4$@$Ni(OH)_2$, $MnCo_2O_4$@$Ni(OH)_2$, $ZnCo_2O_4$, and $MnCo_2O_4$ are determined to be 52, 44.3, 45, and 33.4%, respectively, up to 50 mA cm^{-2}, indicating the higher rate capability of $ZnCo_2O_4$@$Ni(OH)_2$. Indeed, the well-covered ultra-thin $Ni(OH)_2$ nanosheets decrease the path lengths for electrolyte diffusion, increasing electrolyte ion migration during the fast charging-discharging reaction, thereby resulting in the higher rate capability of $ZnCo_2O_4$@$Ni(OH)_2$. Microstructural analysis reveals the development of excess $Ni(OH)_2$ sheets in $MnCo_2O_4$@$Ni(OH)_2$ compared to $ZnCo_2O_4$@$Ni(OH)_2$. The excess $Ni(OH)_2$ nanosheets on $MnCo_2O_4$@$Ni(OH)_2$ comprises a large effective SA; however, the highly dense $Ni(OH)_2$ sheets decrease the electrical conductivity of the hybrid material and prevent the electrolyte access into the core material, resulting in its lower electrochemical performance compared to that of $ZnCo_2O_4$@$Ni(OH)_2$ [19].

To investigate the innate electrochemical behavior (ionic/electrical conductivity) of the as-fabricated electrode material, electrochemical impedance spectroscopy (EIS) analysis was next executed, and the as-obtained Nyquist plots of the four electrodes are shown in Fig. 6e. All four EIS Nyquist spectra comprise a pseudo-semicircle part (high-frequency area) and an approximately straight diagonal line (low-frequency area). The internal resistance (R_s)/charge-transfer resistance (R_{ct}) values of $ZnCo_2O_4$, $ZnCo_2O_4$@$Ni(OH)_2$, $MnCo_2O_4$, and $MnCo_2O_4$@$Ni(OH)_2$ are determined to be 0.74/1.72, 0.61/0.60, 0.82/1.06, and 0.72/0.82 Ω, respectively. These resistance values together with the CV and GCD results confirm the superior electron transport, faster charge-transfer kinetics, and rapid ion penetration at the electrolyte/electrode junction of the core@shell electrode materials [42]. However, compared to the $MnCo_2O_4$@$Ni(OH)_2$ nanohybrids, the $ZnCo_2O_4$@$Ni(OH)_2$ nanohybrids exhibited lower solution resistance and quicker charge-transfer kinetics, owing to its structural advantage. At low frequency, $ZnCo_2O_4$@$Ni(OH)_2$ presented a straight line that is more vertical (higher slope) than those of the other electrode materials. This indicates better electrolyte infiltration (lower ion-diffusion resistance) into the $ZnCo_2O_4$@$Ni(OH)_2$ electrode, resulting in a greater number of rapid redox reactions and higher capacity [5,43].

Another important aspect is the cyclic stability performance measurement of the electrode material to check its durability and quality for practical application. We selected $ZnCo_2O_4$@$Ni(OH)_2$ core@shell electrode for cyclic stability test since it exhibits excellent electrochemical activity. To explore the cyclic performance of the $ZnCo_2O_4$@$Ni(OH)_2$ electrode, the specific capacity was estimated after long-run repeated GCD processes at 40 mA cm^{-2} (Fig. 6f). After 5000 charging and discharging cycles, the retention rate of the initial capacity for $ZnCo_2O_4$@$Ni(OH)_2$ is 90%. The last 15 cycles of the 5000 GCD curves are depicted in the inset of Fig. 6f and indicate that the electrode material maintains its Faradaic battery-type characteristics after 5000 cycles. Additionally, this electrode material shows a Coulombic efficiency of 95–96% across the 5000 cycles, proving its excellent electrochemical activity. On the other hand, the $ZnCo_2O_4$ NWs-based electrode only retains 63.8% capacity after 5000 cycles, attributed to the absence of a protective coating (Fig. S7). The compositional and structural synergies between the $ZnCo_2O_4$ NWs and $Ni(OH)_2$ minimize the dissolution of the electrode material during long cyclic testing, resulting in good electrochemical stability. The free spaces (voids) between the neighboring $Ni(OH)_2$ nanosheets not only act as a perfect "ion reservoir chamber" to accelerate electrolyte diffusion but also prevent the breakdown of the hierarchical architecture, owing to the volume change caused by ion insertion/extraction during the charge-discharge process [8,17,44]. After the cyclic stability test, FESEM (Fig. S8a) analyses were performed to the $ZnCo_2O_4$@$Ni(OH)_2$ electrode material, in order to relate its morphological features to the durability. The FESEM image after cycling test show that the intrinsic morphology of the $ZnCo_2O_4$@$Ni(OH)_2$ electrode is well retained without any significant structural collapse, validating the good mechanical attachment with the current collector. However, the core@shell pattern becomes somewhat weakened after the stability test. Furthermore, the XRD peaks of $Ni(OH)_2$ becomes wider and weaker after the stability test of the core@shell material, as displayed in Fig. S8b. In comparison to the reported binary TMO@$Ni(OH)_x$ (Table S1), $ZnCo_2O_4$@$Ni(OH)_2$ shows superior electrochemical performance (specific capacity and cyclic stability), owing to the following factors: (i) The well-arrayed $ZnCo_2O_4$ NWs serve as a scaffold/support to enable the uniform development of the $Ni(OH)_2$ nanosheets, making the as-formed unique core@shell material completely electrochemically accessible. (ii) A higher amount of $ZnCo_2O_4$ breaks the layered structure of the shell material due to the formation of the undesirable spinel phase of the core material. In the present study, the optimized $ZnCo_2O_4$ NWs played a supportive role to prevent the breakdown of the core@shell assembly during the charging-discharging reaction, (iii) The optimized amount of ultra-thin $Ni(OH)_2$ nanosheets onto the $ZnCo_2O_4$ NWs enhance the unit-cell volume, increase the reversible capacity, and provide well-defined electron transportation pathways during electrochemical reaction. (iv) Maximum capacity contribution from the core material, owing to the easy infiltration of the electrolyte attained by the well-defined $Ni(OH)_2$ shell. (v) The mesoporous network of the as-synthesized hierarchical $ZnCo_2O_4$@$Ni(OH)_2$ material with a high SA and pore volume reduce the ion-diffusion/electron transport pathways and improve the charge storage capability [45].

The ZIF-derived highly porous 3D nitrogen-based carbon material was employed as a favorable negative electrode material to fabricate the solid-state ASC, owing to its excellent conductivity, ultra-high specific SA, and absolute porous morphology [46]. The as-synthesized PNC material was characterized using FESEM, TEM, and BET isotherms. The FESEM image shows that the ZIF-8 sample comprises uniformly distributed rhombic dodecahedral crystals (Fig. 7a) [47,48]. The FESEM images (Figs. 7b, c) of PNC clearly reveal that the original shape (rhombic dodecahedral) of the ZIF-8 nanocrystals is well retained, even after carbonization. The TEM images (Fig. 7d) show the perfect rhombic dodecahedra-based morphology of the PNC material, which is coherent with the FESEM data. The PNC material shows a 3D hierarchical structure with an exclusive porous network and a high specific SA (1600 m^2 g^{-1}; Fig. 7e), which improve the ion transport characteristics during electrochemical study [49].

As a negative electrode in the three-electrode assembly, the PNC electrode shows an excellent electric double-layer-type feature with a quasi-rectangular CV curve under a fixed voltage range (−1.0 to 0 V: Fig. 7f). With the rise in sweep-rate (from 10 to 100 mV s^{-1}), insignificant changes are observed in the shapes/patterns of the CV curves. In addition, the characteristic GCD plots of the PNC electrode material at a variety of areal current densities (2–50 mA cm^{-2}) under a working potential range of −1.0 to 0 V are presented in Fig. 7g. All these GCD plots show near-symmetrical charge-discharge patterns with an insignificant *IR* drop value, suggesting superb Coulombic efficiency and low internal resistance. Furthermore, the linear and triangular shape of the GCD curve indicate typical electrochemical double layer capacitor (EDLC)-type behavior. The plots of the specific capacity values at various current densities are shown in Fig. 7h. The PNC electrode displays specific capacities as high as 49.2, 44.8, 43.2, 42.1, 40.7, 38.4, 36.1, 32.4, 29.5, and 27.0 mA h g^{-1} at 2, 4, 6, 8, 10, 15, 20, 30, 40 and 50 mA cm^{-2}, respectively, indicating a 55% rate performance at 50 mA cm^{-2}. The cyclic stability test of the PNC electrode was performed for 5000 GCD cycles at a current density of 40 mA cm^{-2} (Fig. 7i). Approximately 92%

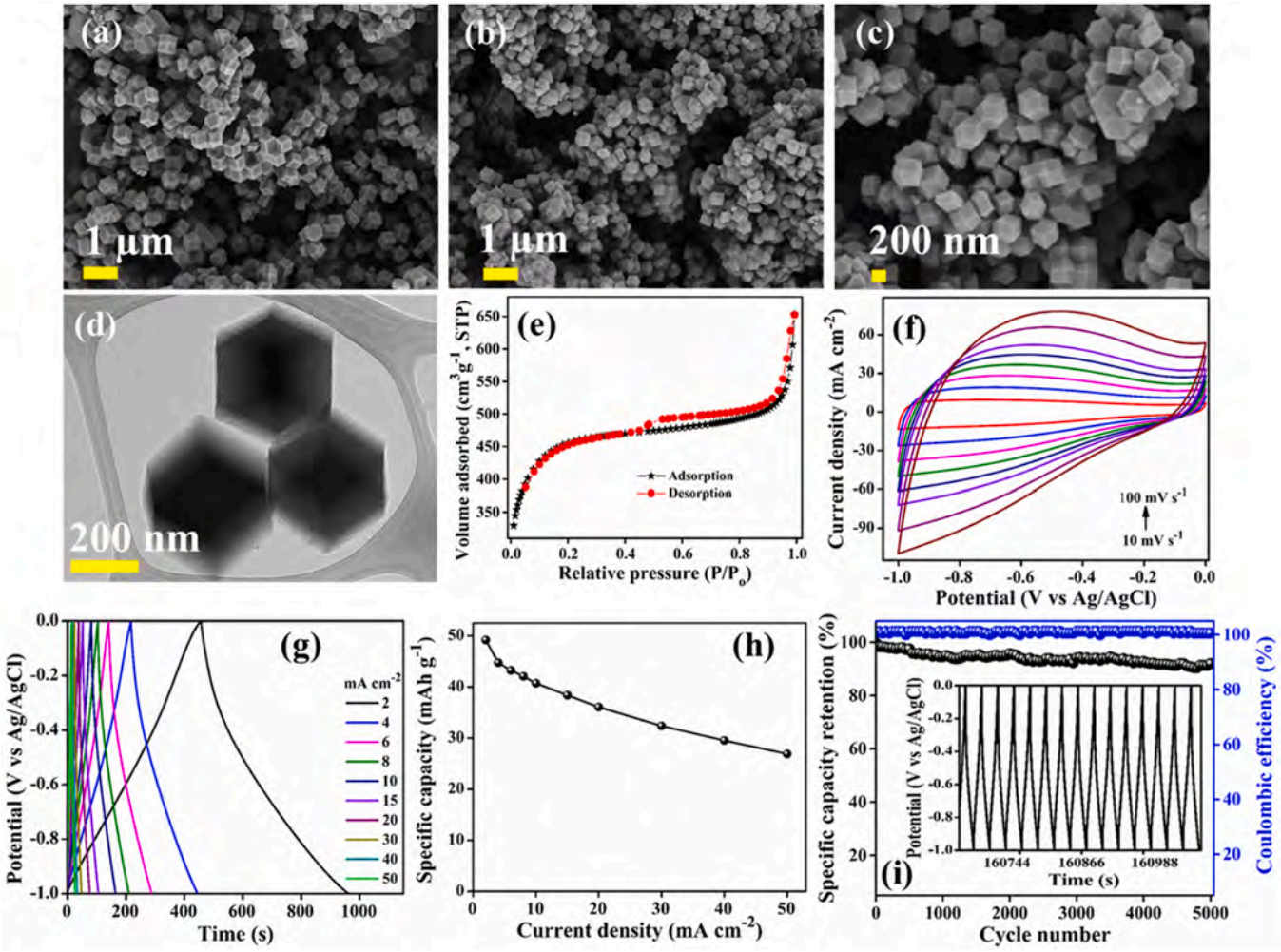

Fig. 7. FESEM images of (a) ZIF-8 and (b,c) PNC, (d) TEM images of PNC, and (e) BET plot of PNC, (f) CV curves, (g) GCD curves, (h) plot of specific capacity at different current densities, and (i) plot of cyclic performance and Coulombic efficiency at a current of 40 mA cm^{-2} (inset: final 15 GCD curve cycles) of the PNC electrode.

of the original capacity is preserved by the PNC electrode after 5000 repeated GCD cycles, representing its outstanding cyclability. Furthermore, the EIS plot attained before the start of cycle testing was compared with that attained after the end of the cycle test to understand the electrochemical properties of the material (Fig. S9). There is no noticeable change in R_s value, while the R_{ct} value increased by ~ 2.7 Ω after the end of the cycle test. These superior electrochemical results indicate the application potential of the PNC as a negative electrode material for solid-state ASC devices.

To further study the possibility for practical utilization of the 3D $ZnCo_2O_4$@$Ni(OH)_2$ hierarchical nanohybrids and 3D PNC materials, ASC device was manufactured from $ZnCo_2O_4$@$Ni(OH)_2$ as positive and 3D porous PNC as negative electrode material using a KOH/PVA gel electrolyte. The CV plots for a three-electrode measuring assembly at a fixed scanning speed of 10 mV s^{-1} for the negative and positive materials are depicted in Fig. 8a. The negative PNC electrode displays near-rectangular features in the CV curve across a potential width range of −1.0 to 0.0 V, confirming EDLC-type behavior. On the other hand, the $ZnCo_2O_4$@$Ni(OH)_2$ nanohybrid sample shows prominent redox peaks within a voltage range of –0.2 to 0.75 V, indicating battery-type character. The digital photographic images of the ASC device ($ZnCo_2O_4$@$Ni(OH)_2$//PNC) constructed using a split test cell are depicted in Fig. S10. The optimum potential window of the ASC device of 1.6 V is selected for electrochemical analysis. The CV plots at separate scan rates ranging from 10 to 50 mV s^{-1} for a fixed potential range of 1.6 V are presented in Fig. 8b. The integrated CV curve area increases with the gradual increase in the scan rate; however, no noticeable changes are observed in the shapes of the typical CV curves. This indicates the high rate of electron transport and suitable capacitive character of the device [22]. The characteristic GCD plots of the ASC device over a fixed voltage range of 0–1.6 V at varied areal current density are shown in Fig. 8c. The symmetrical features of the GCD plots suggest the excellent Coulombic efficiency and good capacitive character of the ASC device. The specific capacity vs current density plot of the device is shown in Fig. 8d. The specific capacity values of the $ZnCo_2O_4$@$Ni(OH)_2$//PNC device are measured to be 97.8, 95.3, 94.7, 92.0, 88.7, 82.4, 76.3, 66.5, 58.0, and 50.5 mA h g^{-1} at 4, 5, 6, 8, 10, 15, 20, 30, 40, and 50 mA cm^{-2}, respectively. Notably, ~52% of the capacity is retained by the device at a high current density of 50 mA cm^{-2}, indicating a good rate capability. Long-term cyclic stability testing (10,000 GCD cycles) of the device was further carried out at 40 mA cm^{-2}. Notably, the device shows a capacity decay of ~14% after 10,000 continuous GCD cycles (Fig. 8e), indicating outstanding cyclic stability. The inset in Fig. 8e depicts the first and last 15 GCD cycles of the total 10,000 cycles. Furthermore, the $ZnCo_2O_4$@$Ni(OH)_2$//PNC device shows excellent Coulombic efficiency (98–99.9%) throughout the cycling test.

The electrical energy storage capability of the ASC solid-state device was elucidated by estimating the energy and power densities. Fig. 8f shows the plot of energy density vs power density, which was identified as a typical Ragone plot. The ASC solid-state device manifests an ultra-

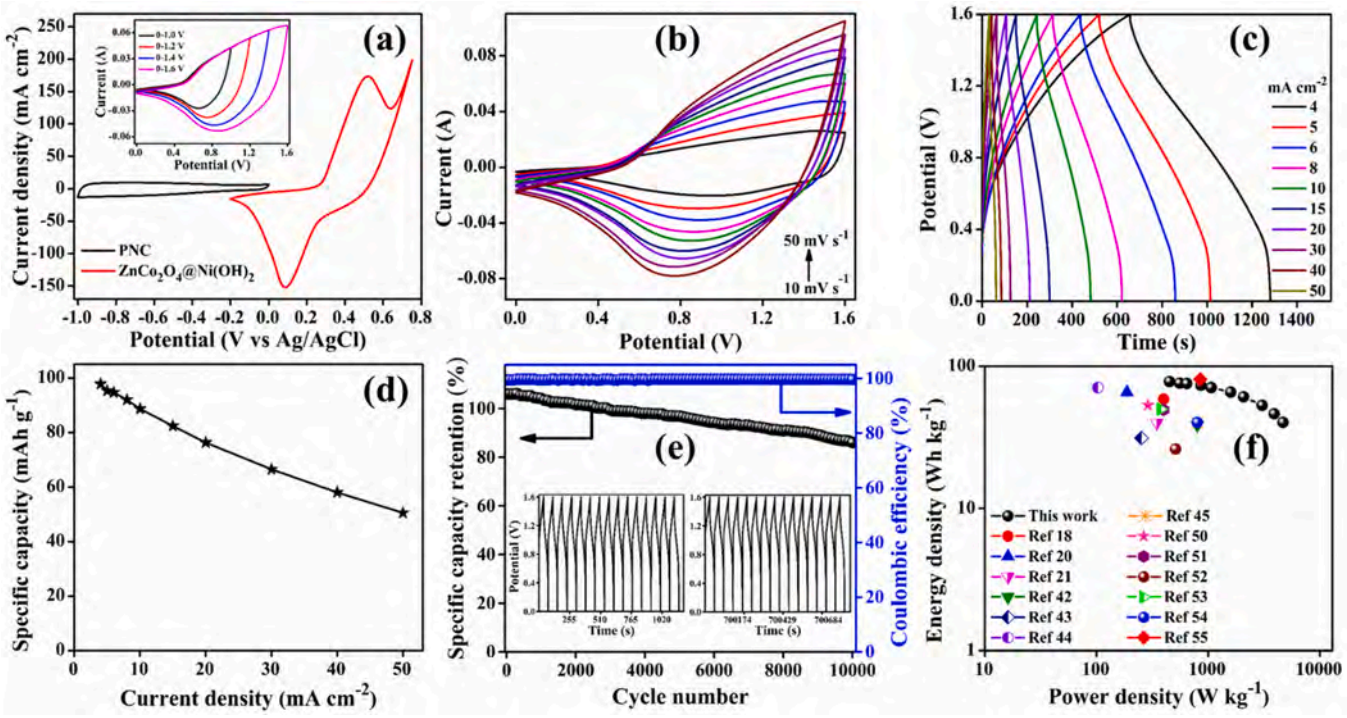

Fig. 8. (a) CV curves of $ZnCo_2O_4$@Ni(OH)$_2$, PNC, and the ASC device at 10 mV s^{-1}. (b) CV curves of the ASC device at various scan rates. (c) GCD curves at various current densities of the ASC device. (d) Plot of specific cell capacity vs current density of the ASC device. (e) Plot of the cyclic stability and Coulombic efficiency at 40 mA cm^{-2} of the ASC device (inset: initial and final 15 cycles). (f) Ragone plot of the ASC device.

high gravimetric energy density of ~78.2 W h kg^{-1} (maximum value) when the power density is 451 W kg^{-1}. Furthermore, the device still delivers ~40.4 W h kg^{-1} energy density at 4691 W kg^{-1} (maximum value) of power density. The above energy and power density values suggest excellent electrochemical performance of the solid-state $ZnCo_2O_4$@Ni(OH)$_2$//PNC device. The electrochemical performance of the solid-state ASC device was compared with the recently reported ASC devices, such as $CuCo_2O_4$@Ni(OH)$_2$/CFC//AC/CFC [18], $CoMoO_4$@Ni(OH)$_2$/OMEP//AC [20], Co_3O_4@Ni(OH)$_2$//AC [21], $CuCo_2O_4$@Ni(OH)$_2$//AC [42], Co_9S_8@Ni(OH)$_2$//AC [43], H-TiO_2@Ni(OH)$_2$//N–C [44], $ZnCo_2O_4$@Ni(OH)$_2$//AC [45], $NiCo_2S_4$@Ni(OH)$_2$//AC [50], NiCoP@C@Ni(OH)$_2$//AC [51], $ZnCo_2O_4$@$Ni_xCo_{2x}(OH)_{6x}$//AC [52], NiCo-LDH/rGO//AC [53], $NiCoO_2$/NiCoP-20//AC [54], $NiCo_2O_4$@NiCo-LDH-G//AC [55], and VN/MoS_2//TiN/MnO_2 [56]. The electrochemical outcome of the as-assembled device outperforms the above reported device systems (Table S2 and Fig. 8f) except $NiCo_2O_4$@NiCo-LDH-G//AC. However, the electrochemical performance of the $NiCo_2O_4$@NiCo-LDH-G//AC [55] device is comparable with our fabricated solid-state ASC device. This outstanding electrochemical storage performance of the $ZnCo_2O_4$@Ni(OH)$_2$//PNC device is attributed to the proper design and assembling of the electro-active materials. Furthermore, the outstanding cooperative interaction within the hierarchical 3D $ZnCo_2O_4$@Ni(OH)$_2$ nanoarrays and highly porous 3D PNC material leads to rapid ion diffusion and electron transfer, resulting in improved electrochemical activity and structural integrity. These results reveal the huge potential of the as-created ASC solid-state device as a favorable advanced energy-storage device.

4. Conclusion

In summary, we have rationally designed and successfully fabricated well-aligned hierarchical MCo_2O_4@Ni(OH)$_2$ (M = Zn or Mn) multi-component core@shell structures on a conductive NF substrate, by changing the core composition using a simple three-step process. Among the as-synthesized MCo_2O_4@Ni(OH)$_2$ nanohybrids, the $ZnCo_2O_4$@Ni(OH)$_2$ nanoarrays show unique nanopine forest-like morphology, high surface area (91 m^2 g^{-1}) and pore volume. The $ZnCo_2O_4$@Ni(OH)$_2$ electrode exhibits a superior supercapacitive performance, with a high specific capacity of 432.6 mA h g^{-1} at 3 mA cm^{-2}, superior capacity retention of 90% after 5000 cycles, and lowest charge-transfer resistance. Furthermore, an ASC solid-state device was designed using $ZnCo_2O_4$@Ni(OH)$_2$ positive electrode and PNC negative electrode. The device exhibits an energy density of 78.2 W h kg^{-1} at 451 W kg^{-1} power density and held a significant energy density of 40.4 W h kg-1 at a high power density of 4691 W kg^{-1}. Our simple and practical synthetic strategy to tune the morphology, physicochemical properties, and electrochemical performance of electro-active materials may stimulate the fabrication of various core@shell architectures, hopefully creating more prospects for energy storage applications.

CRediT authorship contribution statement

Erdenebayar Baasanjav: Conceptualization, Investigation, Methodology, Writing – original draft. **Parthasarathi Bandyopadhyay:** Conceptualization, Methodology, Writing – original draft, Writing – review & editing, Supervision. **Jung Sang Cho:** Formal analysis, Data curation, Validation, Supervision. **Sang Mun Jeong:** Project administration, Writing – review & editing, Supervision.

Declaration of Competing Interest

The authors declare that they have no known competing financial interests or personal relationships that could have appeared to influence the work reported in this paper.

Acknowledgments

This work was supported by the National Research Foundation of Korea (NRF) grant funded by the Korea Government (MSIT) (No. 2019R1A2C1086075; 2021R1A4A2001687). This work was also

supported from Chungbuk National University BK21 program (2021).

References

[1] X. Lu, M. Yu, G. Wang, Y. Tong, Y. Li, Flexible solid-state supercapacitors: design, fabrication and applications, Energy Environ. Sci. 7 (2014) 2160.

[2] J.A. Syed, J. Ma, B. Zhu, S. Tang, X. Meng, Hierarchical multicomponent electrode with interlaced Ni(OH)2 nanoflakes wrapped zinc cobalt sulfide nanotube arrays for sustainable high-performance supercapacitors, Adv. Energy Mater. 7 (2017), 1701228.

[3] E. Baasanjav, P. Bandyopadhyay, G. Saeed, S. Lim, S.M. Jeong, Dual-ligand modulation approach for improving supercapacitive performance of hierarchical zinc–nickel–iron phosphide nanosheet-based electrode, J. Ind. Eng. Chem. 99 (2021) 299–308.

[4] P. Bandyopadhyaya, T.T. Nguyena, N.H. Kima, J.H. Lee, Facile synthesis of 4,4′-diaminostilbene-2,2′-disulfonic-acid-grafted reduced graphene oxide and its application as a high-performance asymmetric supercapacitor, Chem. Eng. J. 333 (2018) 170–184.

[5] P. Bandyopadhyay, G. Saeed, N.H. Kim, S.M. Jeong, J.H. Lee, Fabrication of hierarchical Zn–Ni–Co–S nanowire arrays and graphitic carbon nitride/graphene for solid-state asymmetric supercapacitors, Appl. Surf. Sci. 542 (2021), 148564.

[6] Y. Yuan, W. Wang, J. Yang, H. Tang, Z. Ye, Y. Zeng, J. Lu, Three-dimensional $NiCo_2O_4$@$MnMoO_4$ core−shell nanoarrays for high-performance asymmetric supercapacitors, Langmuir 33 (2017) 10446–10454.

[7] F. Yu, L. Pang, H.-.X. Wang, Preparation of mulberry-like RuO_2 electrode material for supercapacitors, Rare Met. 40 (2021) 440–447.

[8] Y. Zhao, L. Hu, S. Zhao, L. Wu, Preparation of $MnCo_2O_4$@$Ni(OH)_2$ core–shell flowers for asymmetric supercapacitor materials with ultrahigh specific capacitance, Adv. Funct. Mater. 26 (2016) 4085–4093.

[9] V. Augustyn, P. Simon, B. Dunn, Pseudocapacitive oxide materials for high-rate electrochemical energy storage, Energy Environ. Sci. 7 (2014) 1597–1614.

[10] T. Cottineau, M. Toupin, T. Delahaye, T. Brousse, D. Belanger, Nanostructured transition metal oxides for aqueous hybrid electrochemical supercapacitors, Appl. Phys. A 82 (2006) 599–606.

[11] G. Nagaraju, S.C. Sekhar, L.K. Bharat, J.S. Yu, Wearable fabrics with self-branched bimetallic layered double hydroxide coaxial nanostructures for hybrid supercapacitors, ACS Nano 11 (2017) 10860–10874.

[12] P. Bandyopadhyay, G. Saeed, N.H. Kim, J.H. Lee, Zinc-nickel-cobalt oxide@$NiMoO_4$ core-shell nanowire/nanosheet arrays for solid state asymmetric supercapacitors, Chem. Eng. J. 384 (2020), 123357.

[13] R. Patel, J.T. Park, M. Patel, J.K. Dash, E.B. Gowd, R. Karpoormath, A. Mishra, J. Kwak, J.H. Kim, Transition-metal-based layered double hydroxides tailored for energy conversion and storage, J. Mater. Chem. A 6 (2018) 12–29.

[14] Y. Huang, H. Yang, T. Xiong, D. Adekoya, W. Qiu, Z. Wang, S. Zhang, M.-.S. Balogun, J. Tang, Adsorption energy engineering of nickel oxide hybrid nanosheets for high areal capacity flexible lithium-ion batteries, Energy Stor. Mater. 25 (2020) 41–51.

[15] B. Liu, B. Liu, Q. Wang, X. Wang, Q. Xiang, D. Chen, G. Shen, New energy storage option: toward $ZnCo_2O_4$ nanorods/nickel foam architectures for high-performance supercapacitors, ACS Appl. Mater. Interfaces 5 (2013) 10011–10017.

[16] X. Hou, X. Wang, B. Liu, Q. Wang, T. Luo, D. Chen, G. Shen, Hierarchical $MnCo_2O_4$ nanosheet arrays/carbon cloths as integrated anodes for lithium-ion batteries with improved performance, Nanoscale 6 (2014) 8858–8864.

[17] Y.-.L. Liu, C. Yan, G.-.G. Wang, H.-.Y. Zhang, L.-.Y. Dang, B.-.W. Wu, Z.-.Q. Lin, X.-.S. An, J.-.C. Han, Achieving ultrahigh capacity with self-assembled $Ni(OH)_2$ nanosheet-decorated hierarchical flower-like $MnCo_2O_{4.5}$ nanoneedles as advanced electrodes of battery−supercapacitor hybrid devices, ACS Appl. Mater. Interfaces 11 (2019) 9984–9993.

[18] D. Zhu, X. Sun, J. Yu, Q. Liu, J. Liu, R. Chen, H. Zhang, R. Li, J. Yu, J. Wang, Rationally designed $CuCo_2O_4$@$Ni(OH)_2$ with 3D hierarchical core-shell structure for flexible energy storage, J. Colloid Interface Sci. 557 (2019) 76–83.

[19] W. Wu, P. Xia, Y. Xuan, R. Yang, M. Chen, D. Jiang, Hierarchical CoO@$Ni(OH)_2$ core–shell heterostructure arrays for advanced asymmetric supercapacitors, Nanotechnology 31 (2020), 405705.

[20] M. Li, H. Yang, Y. Wang, L. Wang, P.K. Chu, Core-shell $CoMoO_4$@$Ni(OH)_2$ on ordered macro-porous electrode plate for high-performance supercapacitor, Electrochim. Acta 283 (2018) 538–547.

[21] X. Bai, Q. Liu, J. Liu, H. Zhang, Z. Li, X. Jing, P. Liu, J. Wang, R. Li, Hierarchical Co_3O_4@$Ni(OH)_2$ core-shell nanosheet arrays for isolated all-solid state supercapacitor electrodes with superior electrochemical performance, Chem. Eng. J. 315 (2017) 35–45.

[22] M. Liang, M. Zhao, H. Wang, J. Shen, X. Song, Enhanced cycling stability of hierarchical $NiCo_2S_4$@$Ni(OH)_2$@PPy core–shell nanotube arrays for aqueous asymmetric supercapacitors, J. Mater. Chem. A 6 (2018) 2482–2493.

[23] J. Zhang, H. Gao, M.Y. Zhang, Q. Yang, H.X. Chuo, $NiCo_2S_4$/$Ni(OH)_2$ core-shell heterostructured nanotube arrays on carbon-fabric as high-performance pseudocapacitor electrodes, Appl. Surf. Sci. 349 (2015) 870–875.

[24] R. Wang, J. Lang, Y. Liu, Z. Lin, X. Yan, Ultra-small, size-controlled $Ni(OH)_2$ nanoparticles: elucidating the relationship between particle size and electrochemical performance for advanced energy storage devices, NPG Asia Mater 7 (2015) e183.

[25] S. Wang, C. Tan, L. Fei, H. Huang, S. Zhang, H. Huang, X. Zhang, Q.-anA.N. Huang, Y. Hu, H. Gu, Rational design and in-situ synthesis of ultra-thin β-$Ni(OH)_2$ nanoplates for high performance all-solid-state flexible supercapacitors, Front. Chem. 8 (2020), 602322.

[26] L.L. Zhang, H.H. Li, C.Y. Fan, K. Wang, X.L. Wu, H.Z. Sun, J.P. Zhang, A vertical and cross-linked $Ni(OH)_2$ network on cellulose-fiber covered with graphene as a binder free electrode for advanced asymmetric supercapacitors, J. Mater. Chem. A 3 (2015) 19077–19084.

[27] Y. Yan, K. Bao, T. Liu, J. Cao, J. Feng, J. Qi, Minutes periodic wet chemistry engineering to turn bulk Co-Ni foam into hydroxide based nanosheets for efficient water decomposition, Chem. Eng. J. 401 (2020), 126092.

[28] J. Qi, Y. Yan, Y. Cai, J. Cao, J. Feng, Nanoarchitectured design of vertical-standing arrays for supercapacitors: progress, challenges, and perspectives, Adv. Funct. Mater. 31 (2021), 2006030.

[29] Q. Pan, X. Yang, X. Yang, L. Duan, L. Zhao, Synthesis of a MnS/Ni_xS_y composite with nanoparticles coated on hexagonal sheet structures as an advanced electrode material for asymmetric supercapacitors, RSC Adv. 8 (2018) 17754.

[30] H. Cai, X. Li, G. Li, H. Xia, P. Wang, P. Sun, J. Huang, L. Wang, Y. Yang, Synthesis of honeycomb-like nickel-manganese sulfide composite nanosheets as advanced battery-type electrodes for hybrid supercapacitor, Mater. Lett. (255) (2019), 126505.

[31] X. Cao, Y. Liu, Y. Zhong, L. Cui, A. Zhang, J.M. Razal, W. Yang, J. Liu, Flexible coaxial fiber-shaped asymmetric supercapacitors based on manganese, nickel co-substituted cobalt carbonate hydroxides, J. Mater. Chem. A 2020 (2020) 1837.

[32] Y. Li, S. Zhang, M. Ma, X. Mu, Y. Zhang, J. Du, Q. Hu, B. Huang, X. Hua, G. Liu, E. Xie, Z. Zhang, Manganese-doped nickel molybdate nanostructures for high-performance asymmetric supercapacitors, Chem. Eng. J. 372 (2019) 452–461.

[33] T. Hashemi, A.W. Brinkman, X-ray photoelectron spectroscopy of nickel manganese oxide thermistors, J. Mater. Res. 7 (1992) 1278–1282.

[34] Y. Huang, L. Hu, R. Liu, Y. Hu, T. Xiong, W. Qiu, M.-.S. (J. Tang) Balogun, A. Pan, Y. Tong, Nitrogen treatment generates tunable nanohybridization of Ni_5P_4 nanosheets with nickel hydr(oxy)oxides for efficient hydrogen production in alkaline, seawater and acidic media, Appl. Catal. B-Environ. 251 (2019) 181–194.

[35] M.H. Lee, P. Bandyopadhyay, E.M. Jin, E. Baasanjav, D.-.W. Kang, S.M. Jeong, Cathode of Zn-Ni layered double hydroxide nanosheet arrays wrapped with a porous NiMoSx shell and anode of 3D hierarchical nitrogen-doped carbon for high-performance asymmetric supercapacitors, ACS Appl. Energy Mater. 4 (2021) 9166–9177.

[36] S. Li, J. Wen, X. Mo, H. Long, H. Wang, J. Wang, G. Fang, Three-dimensional MnO_2 nanowire/ZnO nanorod arrays hybrid nanostructure for high-performance and flexible supercapacitor electrode, J. Power Sources 256 (2014) 206–211.

[37] R. Kang, W.-.Q. Zhu, S. Li, B.-.B. Zou, L.-.L. Wang, G.-.C. Li, X.-.H. Liu, D.H.L. Ng, J.-.X. Qiu, Y. Zhao, F. Qiao, J.-.B. Lian, Fe_2TiO_5 nanochains as anode for high-performance lithium-ion capacitor, Rare Met. 40 (2021) 2424–2431.

[38] S. Zhou, P. Huang, T. Xiong, F. Yang, H. Yang, Y. Huang, D. Li, J. Deng, M.-S.(J. TangT.) Balogun, Sub-thick electrodes with enhanced transport kinetics via in situ epitaxial heterogeneous interfaces for high areal-capacity lithium ion batteries, Small 17 (2021), 2100778.

[39] G. Li, T. Ouyang, T. Xiong, Z. Jiang, D. Adekoya, Y. Wu, Y. Huang, M.-S.(J. TangT.) Balogun, All-carbon-frameworks enabled thick electrode with exceptional high-areal-capacity for Li-Ion storage, Carbon N Y 174 (2021) 1–9.

[40] B.Y. Guan, A. Kushima, L. Yu, S. Li, J. Li, X.W. Lou, Coordination polymers derived general synthesis of multishelled mixed metal-oxide particles for hybrid supercapacitors, Adv. Mater. 29 (2017), 1605902.

[41] P. Zhang, J. Zhou, W. Chen, Y. Zhao, X. Mu, Z. Zhang, X. Pan, E. Xie, Constructing highly-efficient electron transport channels in the 3D electrode materials for high-rate supercapacitors: the case of $NiCo_2O_4$@$NiMoO_4$ hierarchical nanostructures, Chem. Eng. J. 307 (2017) 687–695.

[42] W. Liu, H. Chen, H. Liao, K. Xiang, W. Chen, X. Li, Self-Supported Sisal-like $CuCo_2O_4$@$Ni(OH)_2$ core−shell composites grown on Ni foam for high-performance all-solid state supercapacitors, Ind. Eng. Chem. Res. 58 (2019) 21233–21241.

[43] F. Zhu, M. Yan, Y. Liu, H. Shen, Y. Lei, W. Shi, Hexagonal prism-like hierarchical Co_9S_8@$Ni(OH)_2$ core–shell nanotubes on carbon fibers for high performance asymmetric supercapacitors, J. Mater. Chem. A 5 (2017) 22782–22789.

[44] Q. Ke, C. Guan, X. Zhang, M. Zheng, Y.W. Zhang, Y. Cai, H. Zhang, J. Wang, Surface-charge-mediated formation of H-TiO_2@$Ni(OH)_2$ heterostructures for high performance supercapacitors, Adv. Mater. 29 (2017), 1604164.

[45] X. Han, Y. Yang, J.-.J. Zhou, Q. Ma, K. Tao, L. Han, C Metal–organic framework templated 3D hierarchical $ZnCo_2O_4$@$Ni(OH)_2$ core–shell nanosheet arrays for high-performance supercapacitors, Chem. Eur. J. 24 (2018) 18106–18114.

[46] Y. An, Y. Tian, Y. Li, S. Xiong, G. Zhao, J. Feng, Y. Qian, Green and tunable fabrication of graphene-like N-doped carbon on a 3D metal substrate as a binder-free anode for high-performance potassium-ion batteries, J. Mater. Chem. A 7 (2019) 21966–21975.

[47] R.R. Salunkhe, C. Young, J. Tang, T. Takei, Y. Ide, N. Kobayashi, Y. Yamauchi, A high-performance supercapacitor cell based on ZIF-8-derived nanoporous carbon using an organic electrolyte, Chem. Commun. 52 (2016) 4764–4767.

[48] X. Gao, X. Liu, D. Wu, B. Qian, Z. Kou, Z. Pan, Y. Pang, L. Miao, J. Wang, Significant role of Al in ternary layered double hydroxides for enhancing electrochemical performance of flexible asymmetric supercapacitor, Adv. Funct. Mater. 29 (2019), 1903879.

[49] Y. An, Y. Tian, Y. Li, C. Wei, Y. Tao, Y. Liu, B. Xi, S. Xiong, J. Feng, Y. Qian, Heteroatom-doped 3D porous carbon architectures for highly stable aqueous zinc metal batteries and non-aqueous lithium metal batteries, Chem. Eng. J. 400 (2020), 125843.

[50] Y. Yang, D. Cheng, S. Chen, Y. Guan, J. Xiong, Construction of hierarchical $NiCo_2S_4$@$Ni(OH)_2$ core-shell hybrid nanosheet arrays on Ni foam for high-performance aqueous hybrid supercapacitors, Electrochim. Acta 193 (2016) 116–127.

[51] Q. Zong, H. Yang, Q. Wang, Q. Zhang, Y. Zhu, H. Wang, Q. Shen, Three-dimensional coral-like NiCoP@C@Ni(OH)$_2$ core-shell nanoarrays as battery-type electrodes to enhance cycle stability and energy density for hybrid supercapacitors, Chem. Eng. J. 361 (2019) 1–11.

[52] W. Fu, Y. Wang, W. Han, Z. Zhang, H. Zha, E. Xie, Construction of hierarchical $ZnCo_2O_4$@$NixCo_{2x}(OH)_{6x}$ core/shell nanowire arrays for high-performance supercapacitors, J. Mater. Chem. A. 4 (2016) 173–182.

[53] L. Zhang, P. Cai, Z. Wei, T. Liu, J. Yu, A.A. Al-Ghamdi, S. Wageh, Synthesis of reduced graphene oxide supported nickel-cobalt-layered double hydroxide nanosheets for supercapacitors, J. Colloid Interface Sci. 588 (2021) 637–645.

[54] W.-.W. Ning, L.-.B. Chen, W.-.F. Wei, Y.-.J. Chen, X.-.Y. Zhang, $NiCoO_2$/NiCoP@Ni nanowire arrays: tunable composition and unique structure design for high-performance winding asymmetric hybrid supercapacitors, Rare Met. 39 (2020) 1034–1044.

[55] S. Wang, Y. Zou, F. Xu, C. Xiang, H. Peng, J. Zhang, L. Sun, Morphological control and electrochemical performance of $NiCo_2O_4$@NiCo layered double hydroxide as an electrode for supercapacitors, J. Energy storage 41 (2021), 102862.

[56] H. Su, T. Xiong, Q. Tan, F. Yang, P.B.S. Appadurai, A.A. Afuwape, M.-S.(Jie J. TangT.) Balogun, Y. Huang, K. Guo, Asymmetric pseudocapacitors based on interfacial engineering of vanadium nitride hybrids, Nanomaterials 10 (2020) 1141.